

Discovery of High-Velocity H-Alpha Above Galactic Center: Testing Models of the Fermi Bubble

DHANESH KRISHNARAO ¹, ROBERT A. BENJAMIN ² AND L. MATTHEW HAFNER ³

¹*Department of Astronomy, University of Wisconsin-Madison, Madison, WI, USA*

²*Department of Physics, University of Wisconsin-Whitewater, Whitewater, WI, USA*

³*Department of Physical Sciences, Embry-Riddle Aeronautical University, Daytona Beach, FL, USA*

(Received 2020 May 29)

Submitted to ApJL

ABSTRACT

Wisconsin H-Alpha Mapper (WHAM) observations reveal high velocity H α and [N II] λ 6584 emission lines in the same direction and velocity as ultraviolet absorption line features that have been previously associated with the biconical gamma-ray lobes known as the Fermi Bubbles. We measure an extinction-corrected intensity of $I_{H\alpha} = 0.84_{-0.09}^{+0.10}$ Rayleigh for emission with line center $v_{\text{LSR}} = -221 \pm 3 \text{ km s}^{-1}$, corresponding to an emission measure of $EM = 2.09_{-0.63}^{+0.64} \text{ cm}^{-6} \text{ pc}$. This emission arises at the same velocity as HST/COS observations of ultraviolet absorption features detected in the PDS 456 quasar sightline that passes through the northern Bubble near $l = 10^{\circ}4, b = +11^{\circ}2$. We estimate the total column density of ionized gas in this velocity component to be $N(H^+) = (3.28 \pm 0.33) \times 10^{18} \text{ cm}^{-2}$. The comparison of ionized gas emission and absorption yields an estimate for the characteristic density of $n_{e,c} = 1.96 \pm 0.63 \text{ cm}^{-3}$ and a characteristic length of $L_c = 0.54 \pm 0.20 \text{ pc}$ assuming 30% solar metallicity. For a temperature of $T_e = 8900 \pm 2700 \text{ K}$ —consistent with the measured line-widths and [N II]/H α line ratio—the gas has a thermal pressure of $p/k = 35,000 \pm 22,000 \text{ cm}^{-3} \text{ K}$. Assuming the gas is $\sim 6.5 \text{ kpc}$ distant, the derived density and pressure appear to be anomalously high for gas $\sim 1.3 \text{ kpc}$ above the Galactic midplane. The large thermal pressure is comparable to both a hot halo or Fermi Bubble model, but suggest that the H α arises in an over-pressured zone.

1. INTRODUCTION

Galactic Center and the interstellar medium (ISM) in its vicinity are a challenge to observe. Dust blocks our view along the Milky Way disk across many wavelengths and images can only provide a 2 dimensional projection on the sky of a complex 3 dimensional foreground, including local features, spiral arms, the bar, and the central molecular zone (CMZ) until finally reaching the super-massive black hole, Sgr A*. Spectroscopy offers a 3D picture of the Galaxy, with radial velocity as the extra dimension. However, models describing the kinematics of the ISM must be used to map these velocities to distances and fully understand the complex nature of the ISM surrounding the nuclear region of the Milky Way.

Initial spectroscopic studies towards Galactic Center, primarily focusing on the 21-cm neutral H I line, re-

vealed the presence of many high velocity emission features near the plane of the Galaxy, suggesting that explosive phenomena were at play (see Oort 1977, for review). Subsequently, much of this gas was explained by unified kinematic models of gas flowing in elliptical streamline orbits (Liszt & Burton 1980), indicating the presence of a bar and removing the need for outflowing gas from the nuclear region. Since we now have observational confirmation of the presence of a strong bar in the Milky Way (see Bland-Hawthorn & Gerhard 2016, for review), many of the high-velocity features near the Galactic midplane can be understood as gas flowing in a bar potential (e.g. Sormani et al. 2018).

The last two decades have seen a resurging interest in the existence of an outflow from the nucleus of the Galaxy. Observations of soft X-rays and radio continuum (Snowden et al. 1997; Sofue 2000; Almy et al. 2000) and later in the mid-infrared and hard X-rays (Bland-Hawthorn & Cohen 2003) were interpreted as emission from gas in the nucleus and bulge of the Galaxy, as were microwave observations of the “Wilkinson Mi-

crowave Anisotropy Probe (WMAP) haze” (Finkbeiner 2004; Dobler & Finkbeiner 2008). The discovery of the “Fermi Bubbles”, large lobes extending $\sim 55^\circ$ above and below the Galactic midplane visible in gamma-ray emission (Su et al. 2010; Dobler et al. 2010; Ackermann et al. 2014), has fueled even more interest in the possibility of Galactic nuclear outflows. Other continuum observations, e.g. polarized synchrotron radiation at radio wavelengths (Carretti et al. 2013), have been interpreted in the context of these gamma-ray results. These observations only provide a 2D image, but their location on the sky towards Galactic Center and relative symmetry across the Galactic plane are argued to support the hypothesis that the emission arises from the center of the Galaxy. Additionally, biconical outflows driven from galactic nuclei are also found in extragalactic systems (Bland & Tully 1988; Cecil et al. 2001; Veilleux & Rupke 2002), where supernovae, stellar winds, or active galactic nuclei can also power large-scale galactic winds (see Heckman 2002, for review).

Of particular interest are spectroscopic observations to measure the kinematics of gas associated with the 2D footprint of the Fermi Bubbles. 21-cm H I observations have shown evidence for neutral gas consistent with a constant velocity Galactic Center outflow (McClure-Griffiths et al. 2013; Di Teodoro et al. 2018; Lockman et al. 2020) within 10° of the midplane. Quasar absorption line spectroscopy was also used to detect signatures of outflowing and infalling gas at high latitudes above and below Galactic Center (Keeney et al. 2006). Later, Fox et al. (2015) used the Hubble Space Telescope (HST) to provide evidence for UV absorption closer to the plane that was interpreted as arising from the front and back side of the northern Fermi Bubble along a single line of sight towards the quasar PDS 456 ($l = 10^\circ.4, b = +11^\circ.2$). This sightline passes through the 1.5 keV emission footprint from Snowden et al. (1997) and does not contain any known high-velocity H I emission (Fox et al. 2015, constrained using the Green Bank Telescope). Since then, more pencil-beam UV sightlines have been studied towards both the northern and southern Fermi Bubbles (e.g. Bordoloi et al. 2017; Karim et al. 2018).

Miller & Bregman (2016) used XMM-Newton and Suzaku X-ray observations of O VII and O VIII emission to model and constrain the properties of a hot gas halo interacting with a large-scale outflow. They found that the energetics involved were consistent with the bubbles forming from a nuclear accretion event at Sgr A*, as opposed to a central star-burst. More recently, Bland-Hawthorn et al. (2019) used HST UV absorption-line ratios from the Magellanic stream to infer the pres-

ence of a Seyfert explosion ~ 3.5 Myr ago, emitting large amounts of ionizing radiation into the conical region of the present day Fermi Bubbles.

Here, we present new WHAM observations of H α and [N II] towards the quasar PDS 456, where high-velocity UV absorption-lines have previously been seen with HST/COS (Fox et al. 2015). These optical spectra provide a new avenue to constrain both the physical conditions of the ionized gas that has been associated with the Fermi Bubbles as well the radiation field emerging from the Galactic Center region and within the Fermi Bubbles. In Section 2, we briefly describe the optical and UV observations. Section 3 explains our analysis methods and presents our new H α and [N II] spectra and the inferred kinematic and physical properties. We discuss these results in Section 4 and summarize our conclusions in Section 5. All data and python notebooks to replicate the results and figures shown are available in the GitHub repository [Deech08/WHAM_PDS456](https://github.com/Deech08/WHAM_PDS456).

2. DATA

2.1. Optical Spectra

Optical spectra were obtained using the Wisconsin H-Alpha Mapper (WHAM; Haffner et al. 2003, 2010, see the WHAM-SS release documentation for details: <http://www.astro.wisc.edu/wham/>), currently located at Cerro-Tololo Inter-American Observatory (CTIO) in Chile. Each 30 – 120 second observation yields a 200 km s^{-1} velocity-range spectrum around H α or [N II] integrated over a 1° beam. The deep spectrum presented here in Figure 1 toward PDS 456 is derived from a total of 112.5 minutes of integration time for H α and 66 minutes for [N II] observed during the summer and early fall of 2019. These spectra are processed using *whampy* (Krishnarao 2019) by applying a flat-field and subtracting an atmospheric template and constant baseline that is fit to the spectra using *lmfit* (Newville et al. 2019). Bright H α sources, such as Sh 2-264 ionized by λ Ori (Sahan & Haffner 2016), are used to apply night-to-night atmospheric corrections to the processed spectra. Several individual observations are then combined using bootstrap resampling to create a continuous, higher signal-to-noise spectrum. Details of the data processing can be found in Haffner et al. (2003). For the deep optical spectra presented here, we estimate a root-mean-square (RMS) error of $0.0015 \text{ R}/(\text{km s}^{-1})$, where $1 \text{ Rayleigh (R)} = 10^6/4\pi \text{ photons s}^{-1} \text{ cm}^{-2} \text{ sr}^{-1}$ and corresponds to an emission measure of $\text{EM} = 2.25 \text{ cm}^{-6} \text{ pc}$ for $T_e = 8000 \text{ K}$ (see Section 3.3).

We have additionally begun a mapping campaign of the sky surrounding PDS 456 at high negative velocities. These pilot observations currently consist of 120-

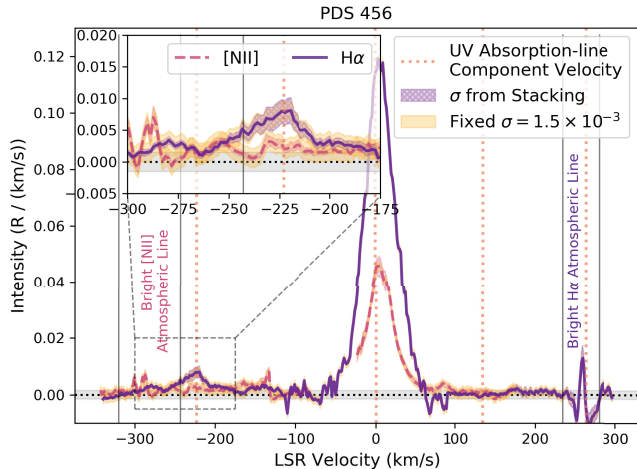


Figure 1. Mean stacked H α (purple) and [N II] (red) emission spectra towards PDS 456 from bootstrap resampling. The yellow shading around the spectra encompass a range of $\pm 0.0015 R/(\text{km s}^{-1})$ while the purple/red hatched shading encompass 1σ errors from bootstrap resampling. A dotted black line and shading run across the $0 \pm 0.0015 R/(\text{km s}^{-1})$ baseline. Dotted orange vertical lines are at the median velocities where UV absorption-line spectra are found at $v_{\text{LSR}} = -223, 0.5, 134.5,$ and 263 km s^{-1} (Fox et al. 2015; Bordoloi et al. 2017). High velocity H α and [N II] emission is detected near the $v_{\text{LSR}} = -223 \text{ km s}^{-1}$ absorption component. the bright emission near $v_{\text{LSR}} = 0 \text{ km s}^{-1}$ is from local gas emission. Only H α observations currently extend beyond $v_{\text{LSR}} = +250 \text{ km s}^{-1}$, but a bright atmospheric line strongly contaminates this velocity range of interest. A bright atmospheric line also contaminates the [N II] spectra between $-320 \text{ km s}^{-1} \lesssim v_{\text{LSR}} \lesssim -243 \text{ km s}^{-1}$, making an accurate measurement of the [N II] emission difficult in its vicinity.

second exposures at each pointing spaced at $\sim 1^\circ$ intervals and are processed in the same way as described above, but without the final stacking of several spectra. This results in slightly noisier spectra with RMS errors of $\sim 0.01 R/\text{km s}^{-1}$ and will be discussed further in Section 4.

2.2. UV Spectra

We also use the UV spectra towards PDS 456 originally presented in Fox et al. (2015), with Voigt-profile fitting results from Bordoloi et al. (2017, see their Table 2). The observations were originally taken in 2014 from the Cosmic Origins Spectrograph (COS Green et al. 2012) on HST using the G130M setting centered on 1291\AA and G160M setting centered on 1600\AA . These spectra have a $FWHM = 20 \text{ km s}^{-1}$ spectral resolution with an absolute velocity calibration accurate to within 5 km s^{-1} and a signal-to-noise of $\sim 12 - 20$ per resolution element. For full details on these spec-

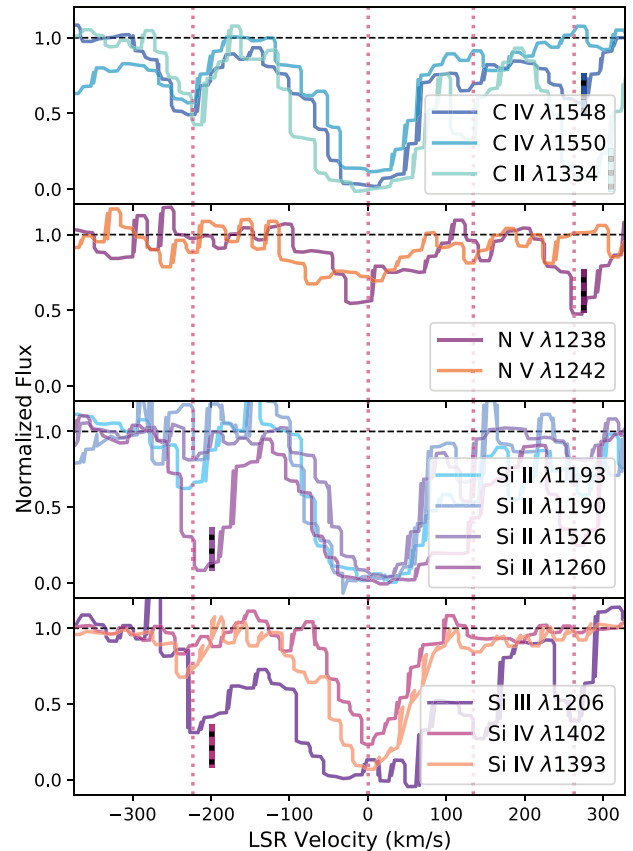


Figure 2. Normalized UV Absorption line spectra from HST/COS towards PDS 456, showing different carbon, nitrogen, and silicon ions from top to bottom. The dotted red vertical lines are at the velocities where UV absorption-line spectra are found as in Figure 1. This figure is reproduced from Fox et al. (2015, their Figure 2). Some absorption components, such as the Si III line near -200 km s^{-1} are contaminated by other red-shifted transitions, with these features marked with dashed-black vertical lines (see Fox et al. 2015; Bordoloi et al. 2017, for details)

tra and their processing, see Fox et al. (2014, 2015) and Bordoloi et al. (2017). In this work, we display UV spectra rebinned to match one resolution element, but the Voigt-profile fitting from Fox et al. (2015) and Bordoloi et al. (2017) is done on the unbinned data. Select spectra are shown in Figure 2. While there is no detection of N V absorption, 3σ upper limits are estimated using the RMS noise of the spectra to be $\log(N_{\text{NV } \lambda 1238}) < 14.10$ and $\log(N_{\text{NV } \lambda 1242}) < 14.15$ (Fox 2020, priv. comm.).

3. METHODS AND RESULTS

We use a combination of new optical emission lines and previously measured UV absorption lines to constrain the temperature, density, and pressure of high-

velocity gas features. Here we briefly describe our methods of deriving these constraints.

3.1. Optical Line Measurements

We measure integrated intensities, velocity centroids, and line widths of $H\alpha$ and $[N II]$ emission lines focusing on the high-negative velocity region between $-270 \text{ km s}^{-1} < v_{\text{LSR}} < -200 \text{ km s}^{-1}$. Integrated intensities are computed with the standard “zereth moment”, while velocity centroids and line widths are derived using the method proposed in [Teague & Foreman-Mackey \(2018\)](#). This method more accurately identifies velocity centroids and uncertainties by fitting a quadratic model to the brightest pixel and its two nearest neighbors in a spectrum. The line width is estimated using a ratio of the peak intensity identified in the above step and the zeroth moment, assuming a Gaussian line profile. This method is preferable to the traditional first and second moments or parameters estimated through Gaussian component fitting because of our relatively low signal-to-noise. Before finding velocity centroids and line widths, the data is first smoothed using a Savitzky-Golay filter ([Savitzky & Golay 1964](#)) with a width of $\sim 4 \text{ km s}^{-1}$.

The optical spectra are shown in [Figure 1](#), with the velocity region of interest enlarged. The emission near $v_{\text{LSR}} = 0 \text{ km s}^{-1}$ is from local emission. The high negative velocity emission is centered at $v_{\text{LSR}} = -221 \pm 5 \text{ km s}^{-1}$ for $H\alpha$ and $v_{\text{LSR}} = -230 \pm 5 \text{ km s}^{-1}$ for $[N II]$, with observed integrated intensities of $I_{H\alpha} = 0.287 \pm 0.014 R$ and $I_{NII} = 0.077 \pm 0.011 R$ and line widths of $\sigma_v = 14.1 \pm 2.7 \text{ km s}^{-1}$ for $H\alpha$ and $\sigma_v = 9.6 \pm 4.5 \text{ km s}^{-1}$ for $[N II]$. Throughout this work, we use σ_v , the standard deviation, to describe line widths.

3.2. Temperature and Non-Thermal Broadening

We assume the ions observed using both HST/COS (C II, Si II, Si IV) and WHAM ($[N II]$, H II) are at thermal equilibrium with one another, exhibiting the same gas temperatures and experiencing the same input of turbulence and non-thermal broadening mechanisms. We do not consider the Si III and C IV absorption line widths due to contamination from other red shifted transitions or skewed absorption profiles which lead to poor estimates from Voigt profile fits. Then the line widths of these ions are modeled as a function of the ionized gas temperature, T_e , mass, m , and a non-thermal broadening component, σ_{nonT} using

$$\sigma_{model}(T_e, m, \sigma_{nonT}) = \sqrt{\left(\frac{2k_B T_e}{m} + \sigma_{nonT}^2\right)} \quad (1)$$

The warm gas temperature and non-thermal broadening component are constrained using a Bayesian Markov

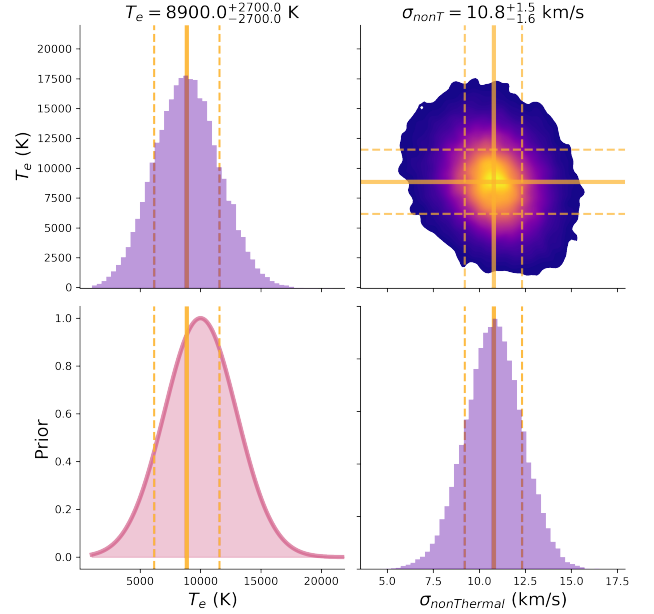


Figure 3. Posterior distributions from MCMC fitting of emission line width models assuming a thermal and non-thermal broadening term with a flat prior on non-thermal broadening and a Gaussian prior on the ionized gas temperature. The Gaussian prior for the temperature is shown in red on the lower left panel. The diagonal panels show marginalized histograms (purple), with the median (solid) and 16th and 84th percentile values (dashed) shown in yellow for the gas temperature and non-thermal broadening term. The upper right panel shows a 2D Gaussian kernel density estimate of both parameters.

Chain Monte Carlo (MCMC) approach implemented using [emcee \(Foreman-Mackey et al. 2013\)](#). We use a flat prior on σ_{nonT} constrained between $1 \text{ km s}^{-1} < \sigma_{nonT} < 20 \text{ km s}^{-1}$ and a Gaussian prior on T_e with a mean of 10^4 K and standard deviation of 3000 K , limited to a range of $10^3 \text{ K} < T_e < 10^5 \text{ K}$. Our likelihood, \mathcal{L} , has the form

$$\log(\mathcal{L}) = -1/2 \sum_{ions} \left[\frac{(\sigma_{obs,ion} - \sigma_{model,ion}(m_{ion}))^2}{s_{obs,ion}^2} + \log(s_{obs,ion}^2) \right] \quad (2)$$

where $\sigma_{obs,ion}$ is the observed line width of an ion, $s_{obs,ion}$ is the standard error of the observed line width, and m_{ion} is the atomic mass. Parameter values are derived from the median of the posterior probability distributions after 10,000 steps, with the 16th and 84th percentiles used to estimate errors. The resulting gas temperature and non-thermal broadening contribution are $T_e = 8900 \pm 2700 \text{ K}$ and $\sigma_{nonT} = 10.8^{+1.5}_{-1.6} \text{ km s}^{-1}$, with posterior distributions shown in [Figure 3](#).

3.3. Extinction Corrections

In order to correct the optical line emission for extinction we use the 3D dust maps of [Green et al. \(2019\)](#) and a ([Fitzpatrick & Massa 2007](#)) extinction curve. We adopt the [Di Teodoro et al. \(2018\)](#) kinematic model, which places the emission at a distance of $D = 6.5 \pm 0.08$ kpc. To account for the large uncertainty in constraining actual 3D distances, we use a distance of $D = 6.5 \pm 0.2$ kpc. We estimate A_V using 10,000 points distributed uniformly in position within our beam and distributed as a Gaussian around our estimated distance, resulting in $A_V = 1.5 \pm 0.2$ mag.

The extinction corrected intensities are then $I_{H\alpha} = 0.84_{-0.09}^{+0.10}$ R and $I_{\text{NII}} = 0.225_{-0.025}^{+0.028}$ R. The resulting extinction corrected [N II]/H α line ratio is [N II]/H $\alpha = 0.26 \pm 0.05$. Assuming case B recombination and no absorption, H α surface brightness can be related to the emission measure, $EM = \int_0^\infty n_e^2 ds$ as

$$EM = (2.77 \text{ cm}^{-6} \text{ pc}) \left(\frac{I_{H\alpha}}{R} \right) \times T_4^{(0.942+0.031 \ln T_4)} \quad (3)$$

where $T_4 = T_e/10^4$ K, and the constant term is derived from the effective recombination rate of H α ([Draine 2011](#)). At the inferred temperature of $T_e = 8900 \pm 2700$ K, the extinction corrected emission measure is $EM = 2.09_{-0.63}^{+0.64} \text{ cm}^{-6} \text{ pc}$. A summary of the measured optical emission and UV absorption line properties are shown in Table 1.

3.4. Ionized Gas Column Density

We estimate the ionized gas column density using the silicon absorption line measurements, assuming that all silicon gas is either singly, doubly, or triply ionized, and at a single gas temperature. The constrained upper limit on the H I column density towards PDS 456 of $N_{\text{HI}} < 3.3 \times 10^{17} \text{ cm}^{-2}$ ([Fox et al. 2015](#)) supports this fully ionized assumption. The ionized gas column density is then

$$N_{\text{H}^+} = \frac{N_{\text{SiII}} + N_{\text{SiIII}} + N_{\text{SiIV}}}{(\text{Si}/\text{H})} \quad (4)$$

where (Si/H) is the silicon abundance.

The combination of emission, probing the warm ionized gas density squared, and absorption, probing the ionized gas column density, allows for the ionized gas density to be solved for using

$$n_e = (0.32 \text{ cm}^{-3}) \left(\frac{EM}{\text{cm}^{-6} \text{ pc}} \right) \left(\frac{N_{\text{H}^+}}{10^{18} \text{ cm}^{-2}} \right)^{-1} \quad (5)$$

This estimate of n_e has no dependence on the path length, L , of emitting/absorbing gas. L can instead be

derived as

$$L = (9.62 \text{ pc}) \left(\frac{N_{\text{H}^+}}{10^{18} \text{ cm}^{-2}} \right)^2 \left(\frac{EM}{\text{cm}^{-6} \text{ pc}} \right)^{-1} \quad (6)$$

The thermal pressure is approximately $p/k = 2 n_e T_e$ where the factor of 2 accounts for the fact that the gas is fully ionized.

Assuming a solar metallicity of $(\text{Si}/\text{H})_\odot = (3.24 \pm 0.22) \times 10^{-5}$ ([Asplund et al. 2009](#)) and no depletion onto dust grains, Equation 4 yields $N_{\text{H}^+} = (9.85 \pm 0.99) \times 10^{17} \text{ cm}^{-2}$. Combining with the the extinction corrected emission measure results in estimates of the characteristic ionized gas density and length of $n_e = 6.5 \pm 2.1 \text{ cm}^{-3}$ and $L = 0.05 \pm 0.02 \text{ pc}$. These in turn provide an estimate of the thermal gas pressure, $p/k = 116,000 \pm 70,000 \text{ cm}^{-3} \text{ K}$.

A principal caveat for these estimates is that they are derived by comparing pencil-beam absorption measurements with a one-degree beam for emission. If the observed column density is significantly below the average column density in the one-degree solid angle, it will produce overestimates of the density and pressure.

3.5. Metallicity Effects

The total ionized gas column density we estimate depends on the gas phase metallicity, Z , as shown in Equation 4. As a result, our estimated ionized gas density and thermal pressure are linearly proportional to the metallicity, while the path length is $L \propto 1/Z^2$. [Bordoloi et al. \(2017\)](#) estimates the outflowing gas has a sub-solar metallicity of $Z \gtrsim 30\%$ based on photoionization modelling and O I/H I measurements towards 1H1613-097, a different quasar line of sight passing through the northern Fermi Bubble. Additionally, [Keeney et al. \(2006\)](#) estimated metallicities of $\gtrsim 10 - 20\%$ solar for other high velocity clouds towards Galactic Center.

Our measure of the [N II]/H α line ratio can serve as an independent check of the sub-solar metallicity estimate. N^+ and H^+ have similar first ionization potentials of 14.5 eV and 13.6 eV, respectively. As a result, they often exhibit similar ionization levels in photoionized gas such that $N^+/N^0 \approx H^+/H^0$ ([Haffner et al. 1999](#)). Then the ratio can be expressed

$$[\text{N II}]/\text{H}\alpha = (1.63 \times 10^5) \left(\frac{N}{H} \right) T_4^{0.426} e^{-2.18/T_4} \quad (7)$$

where $(\frac{N}{H})$ is the nitrogen abundance. Photoionization models predict $N^+/N^0 \sim 0.8 \times H^+/H^0$ ([Sembach et al. 2000](#)), which would decrease the [N II]/H α line ratio by 20%.

With a solar nitrogen abundance of $(\text{N}/\text{H})_\odot = (6.76 \pm 0.78) \times 10^{-5}$ ([Asplund et al. 2009](#)), and our

Ion	Instrument	v_{LSR}	Intensity	Intensity	$\log(N)$	σ_v
		(km s^{-1})	(R)	[Dereddened] (R)	(cm^{-2})	(km s^{-1})
H I/21-cm ^a	GBT				< 17.48	N/A
H II/H α	WHAM	-221 ± 5	0.287 ± 0.014	$0.84^{+0.10}_{-0.09}$		14.1 ± 2.7
[N II]	WHAM	-230 ± 5	0.077 ± 0.011	$0.225^{+0.028}_{-0.025}$		9.6 ± 4.5
Si II	HST/COS	-223 ± 2			13.02 ± 0.08	9.3 ± 2.8
Si III ^b	HST/COS	-197 ± 2			13.13 ± 0.02	27.8 ± 1.6
Si IV	HST/COS	-231 ± 2			12.9 ± 0.06	13.4 ± 2.4
C II	HST/COS	-220 ± 6			13.8 ± 0.14	14.1 ± 5.7
C IV	HST/COS	-233 ± 2			13.79 ± 0.03	22.6 ± 1.5
N V ^c	HST/COS	N/A			< 14.10	N/A
H I/21-cm ^a	GBT				< 17.48	N/A
H II/H α ^d	WHAM	N/A	< 1.24	N/A		N/A
Si II	HST/COS	264 ± 2			13.37 ± 0.02	25.1 ± 1.6
Si III	HST/COS	259 ± 2			12.85 ± 0.04	12.9 ± 1.6
Al II	HST/COS	263 ± 3			13.53 ± 0.63	0.6 ± 2.1

^a 3σ upper limit from (Fox et al. 2015) constrained with the Green Bank Telescope (GBT).

^b Partial Ly β contamination at $z = 0.175539$.

^c 3σ upper limit

^d 3σ upper limit coincident with a bright atmosphere line (see Section 3.6).

Table 1. Measured emission and absorption line centroids, intensities, column densities, and velocity widths from WHAM (this work) and HST/COS (Fox et al. 2015; Bordoloi et al. 2017). Extinction corrections use 3D dust models from Green et al. (2019) and assume a distance of 6.5 ± 0.2 kpc.

estimated gas temperature, $T_e = 8900 \pm 2700$ K, the predicted line ratio from Equation 7 is $[\text{N II}]/\text{H}\alpha = 0.91 \pm 0.80$, with the large error resulting from the large error on T_e . If instead, we consider 30% solar nitrogen abundance, then $[\text{N II}]/\text{H}\alpha = 0.27 \pm 0.24$. While both can be consistent with our measured line ratio of $[\text{N II}]/\text{H}\alpha = 0.26 \pm 0.05$ due to the uncertainty in estimated temperatures, our relatively low measured line ratio could better support a sub-solar metallicity as suggested in Bordoloi et al. (2017).

At 30% metallicity, our measured ionized column is $N_{\text{H}^+} = (3.28 \pm 0.33) \times 10^{18} \text{ cm}^{-2}$, resulting in $n_e = 1.96 \pm 0.63 \text{ cm}^{-3}$, $L = 0.54 \pm 0.20$ pc, and $p/k = 35,000 \pm 22,000 \text{ cm}^{-3} \text{ K}$.

3.6. High Positive Velocity Components

We detect no significant H α or [N II] emission around $v_{\text{LSR}} \sim +135 \text{ km s}^{-1}$ where UV absorption is observed. 3σ upper limits for H α and [N II] for this component using an RMS noise of $0.0015 R / (\text{km s}^{-1})$ are both $0.124 R$. Since the dust is primarily limited to the foreground in 3D models, we assume the same $A_V = 1.5 \pm 0.2$ mag from Green et al. (2019). Then assuming the same gas temperature as above, our extinction corrected emission measure upper limit is $EM < 0.90 \pm 0.28 \text{ cm}^{-6} \text{ pc}$. Combined with UV absorption col-

umn densities from Bordoloi et al. (2017) yields $n_e < (1.9 \pm 0.6 \text{ cm}^{-3})^{Z/Z_\odot}$, $L > (0.25 \pm 0.10 \text{ pc})^{(Z/Z_\odot)^{-2}}$, and $p/k < (34,000 \pm 22,000 \text{ cm}^{-3} \text{ K})^{Z/Z_\odot}$, where Z is the metallicity.

Bright OH line contamination from the upper atmosphere in our H α spectrum coincides with the UV absorption feature near $v_{\text{LSR}} \sim +263 \text{ km s}^{-1}$. Larger residuals from this line are seen in Figure 1 near $v_{\text{LSR}} \sim +260 \text{ km s}^{-1}$. Also, our current [N II] observations do not extend to this high positive velocity region. We can estimate an approximate 3σ upper limit for H α emission at the high positive velocity component using an enhanced RMS noise of $0.015 R / (\text{km s}^{-1})$ to be $I_{\text{H}\alpha} < 1.24 R$.

4. DISCUSSION

High-velocity ultraviolet absorption lines detected in sightlines towards the inner Galaxy have previously been interpreted in the context of an outflow associated with the Fermi Bubble. The addition of optical emission line observations provides a test of this hypothesis. If the UV absorbing and H α emitting gas originates at a hydrodynamic interface between the outflowing Fermi Bubbles and ambient halo gas, we would expect two key signatures: (1) gas at high pressures, and (2) a bipolar geometry with velocity gradients as a function

of latitude and longitude. Our H α observations towards PDS 456 indicate that the first signature is indeed present; the measured thermal pressure is anomalously high for warm ionized gas ~ 1.3 kpc above the Galactic midplane. In the solar neighborhood, assuming a midplane density of $n_{e,0} = 0.03 - 0.08 \text{ cm}^{-3}$ and scale-height of $1.0 - 1.8$ kpc, warm ionized gas with temperature $T_e = 8000$ K located 1.3 kpc above the plane would only have a thermal pressure of $p/k \sim 100 - 600 \text{ cm}^{-3} \text{ K}$. Savage et al. (2017) measured a thermal pressure of $p/k \sim 10^5 \text{ cm}^{-3} \text{ K}$ in an ultraviolet absorption component detected at -114 km s^{-1} in the spectrum of LS 4825, a B1 Ib-II star at distance of ~ 21 kpc. Assuming this absorption arises in the vicinity of Galactic Center, the gas is ~ 1 kpc below the Galactic plane.

Our derived pressures of the warm ionized gas are comparable to the thermal pressure predicted by models of hot, X-ray emitting gas surrounding the Galaxy. A model of the Milky Way’s hot halo based on an analysis of O VII and O VIII X-ray emission lines (Miller & Bregman 2015) predicts a density and pressure of $n_e = 3 \times 10^{-3} \text{ cm}^{-3}$ and $p/k = 12,000 \text{ cm}^{-3} \text{ K}$ at the modelled distance. It also predicts a pressure of $p/k \sim 54,000 \text{ cm}^{-3} \text{ K}$ for the high-pressure component seen towards LS 4825, assuming a solar metallicity. In a follow-up work, they incorporated a Fermi Bubble shell model and intended to explain an excess of O VII and O VIII X-ray emission in the inner Galaxy (Miller & Bregman 2016). This work yielded a shell temperature of $\log T_e/K = 6.7^{+0.25}_{-0.1}$ and density $n_e = (10 \pm 0.3) \times 10^{-4} \text{ cm}^{-3}$, corresponding to a thermal pressure $p/k = 10,000^{+19,000}_{-3000} \text{ cm}^{-3} \text{ K}$ at solar metallicity (Miller & Bregman 2016)¹. The fraction of their $L_{\text{Hot}} = 1$ kpc shell occupied by warm ionized gas with our characteristic length of $L_{\text{Warm}} = 0.54 \pm 0.20$ pc is $L_{\text{Hot}}/L_{\text{Warm}} = (5.4 \pm 2.0) \times 10^{-4}$.

The concordance between our thermal pressure estimates and the expected thermal pressure of a hot gas halo supports the hypothesis that the observed absorption is associated with warm ionized gas above the central Galaxy. Uncertainties in our thermal pressure measurements, combined with the uncertainties in the pressure estimate of the hot halo and Fermi Bubble shell, do not allow us to say whether the gas arises in the bipolar shell of a nuclear outflow or from gas embedded in a hot medium, similar to the observed HI (McClure-Griffiths et al. 2013; Di Teodoro et al. 2018; Lockman et al. 2020).

While UV absorption line observations are limited by the availability of background targets and 21-cm observations sparsely sample the volume, mapping extended optical line emission has the potential to trace the continuity of gas kinematics above and below the inner Galaxy. To this end, we initiated a campaign to spectroscopically map the sky at high velocities surrounding the footprint of the Fermi Bubbles. In Figure 4, we show early results from mapping a small region surrounding PDS 456 at high, negative velocities. The top-right panel shows a synthetic map of H α from a constant surface brightness slab of gas at $D = 6.5$ kpc after applying extinction from 3D estimates (Green et al. 2019). We see evidence for extended emission at high, negative velocities in the vicinity of PDS 456, shown in the top-left panel. Velocity centroids of the emitting gas are shown in the lower panel. These velocity estimates have large errors and currently show no strong evidence for a gradient as predicted in kinematic outflow models (e.g. Bordoloi et al. 2017; Di Teodoro et al. 2018) or seen in H I observations (Lockman et al. 2020). Future work and continued WHAM observations will allow this initial map to be expanded and better confront model predictions.

In the future, our H α observations close to, or from within the boundaries of the Fermi Bubble can also provide an opportunity to constrain the radiation field emerging from Galactic Center. Previously, H α observations from the Wisconsin H-Alpha Mapper (WHAM) of ionized gas in the Magellanic stream have been used to diagnose the radiation field emerging from Galactic Center ~ 4 Myr ago (Bland-Hawthorn et al. 2013; Barger et al. 2017). The smaller distance to Galactic Center for the gas we discuss here would provide a much more recent glimpse into the ionizing radiation field emerging from Sgr A* and the CMZ, as well as more localized ionization sources, such as shocks or cooling flows.

5. CONCLUSIONS

We have discovered high-velocity optical emission in the vicinity of the 2D footprint of the Fermi Bubbles at the same velocity as previously observed UV absorption features (Fox et al. 2015). As a result, we have measured model-independent constraints on the *in-situ* physical conditions of warm gas above Galactic Center toward the quasar PDS 456. We summarize our findings to be

1. H α and [N II] emission are detected at high negative velocity with extinction-corrected intensities of $I_{\text{H}\alpha} = 0.84^{+0.10}_{-0.09} \text{ R}$ and $I_{[\text{NII}]} = 0.225^{+0.028}_{-0.025} \text{ R}$.
2. Optical emission and UV absorption from low ions have line widths indicating a gas temperature of

¹ Since Miller & Bregman (2016) report hydrogen particle density, we multiply by two to get the total particle density of fully ionized gas.

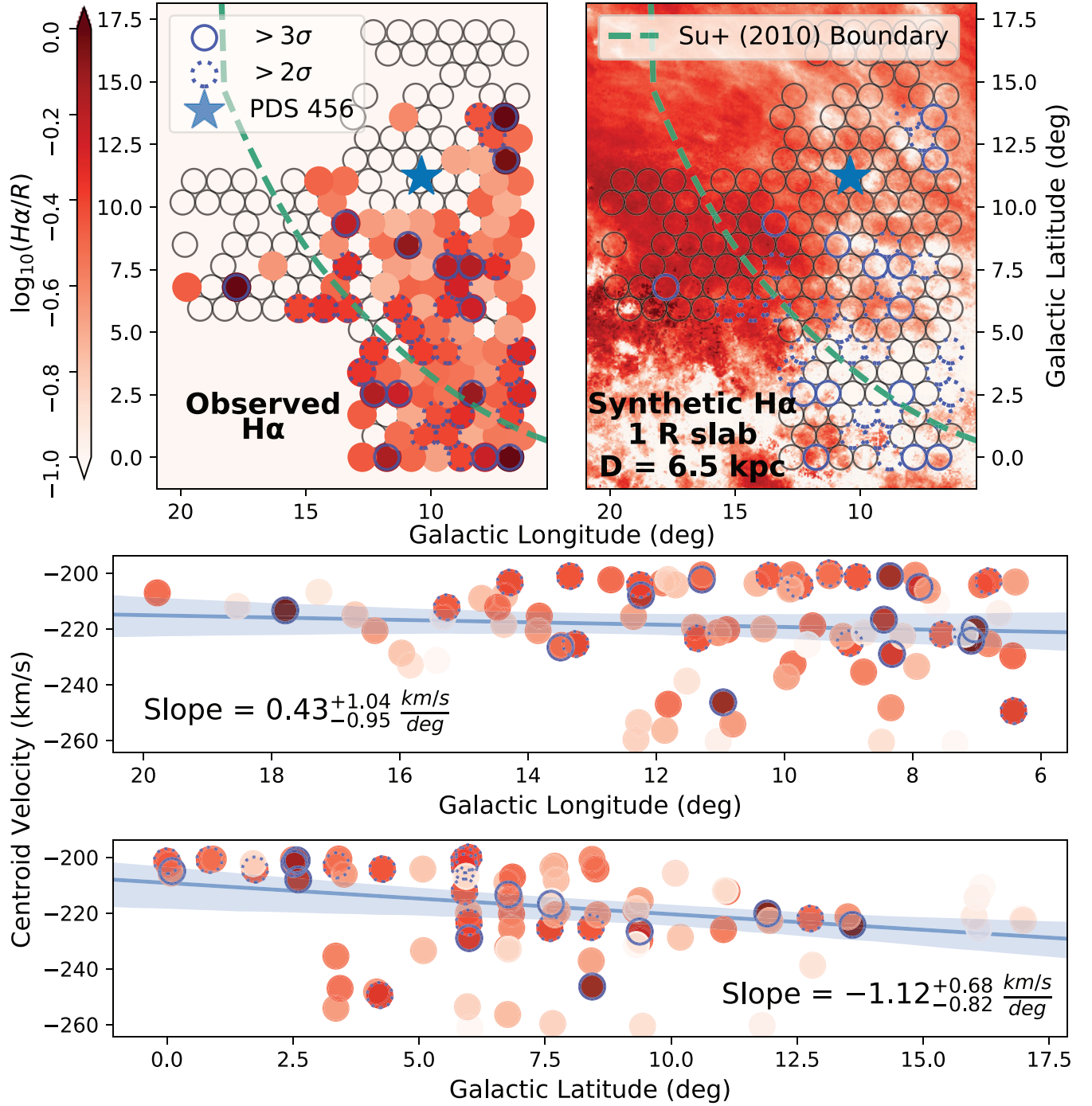


Figure 4. Preliminary H α map surrounding the PDS 456 quasar composed of 120s exposures per pointing integrated between $-270 \text{ km s}^{-1} < v_{\text{LSR}} < -200 \text{ km s}^{-1}$ (*top-left*). Only pointings above a 1σ detection threshold are colored by their intensity, while open circles show the location of pointings with no detected emission. 2σ and 3σ detections are further outlined with blue, dotted and solid outlines, respectively. A synthetic H α image of a slab with uniform H α surface brightness of 1 R is shown after applying dust attenuation as predicted from [Green et al. \(2019\)](#), with the WHAM beams shown as open circles (*top-right*). A green dashed line marks the approximate outline of the northern Fermi Bubble from [Su et al. \(2010\)](#). Velocity centroids as a function of Galactic longitude (*middle*) and Galactic latitude (*bottom*) are shown for measurements with errors $< 12 \text{ km s}^{-1}$. On average, the plotted velocity centroids have standard errors of 8 km s^{-1} . Robust least-squares linear-regression fits are shown in blue with 95% confidence intervals from 1000 bootstrap re-samples.

$T_e = 8900 \pm 2700$ K with a non-thermal contribution of $\sigma_{nonT} = 10.8_{-1.6}^{+1.5}$ km s $^{-1}$.

3. The observed optical line ratio of $[\text{N II}]/\text{H}\alpha = 0.26 \pm 0.05$ is consistent with abundances of approximately 30% solar when compared to an estimate of the gas metallicity towards a different sightline probing the northern Fermi Bubble (Bordoloi et al. 2017).
4. Assuming 30% solar metallicity, the ionized gas has a characteristic density and length of $n_e = 1.96 \pm 0.63$ cm $^{-3}$ and $L_e = 0.54 \pm 0.20$ pc with a thermal pressure of $p/k = 35,000 \pm 22,000$ cm $^{-3}$ K. This high thermal pressure is comparable to, but still greater than, those predicted by models of a hot gas halo in the inner Galaxy or of a Fermi Bubble shell (Miller & Bregman 2015, 2016).
5. Initial H α spectroscopic maps of the region surrounding PDS 456 reveal extended emission at the same high, negative velocities.

With future observations, WHAM can trace emission associated with the Fermi Bubbles both spatially and kinematically at large scales. Additionally, other pointed observations towards distant UV bright sources with existing HST spectra can provide sensitive column-density profiles of multiple species across different regions of the southern and northern Fermi Bubbles.

ACKNOWLEDGMENTS

We thank Andrew Fox for providing useful comments and constraints on the UV absorption line measurements and total ionized gas column density. We acknowledge the support of the U.S. National Science Foundation (NSF) for WHAM development, operations, and science activities. The optical observations and work presented here were funded by NSF awards AST-0607512, AST-1108911, AST-1714472/1715623, and AST-1940634. RAB would like to acknowledge support from NASA grant NNX17AJ27G. Some of this work took part under the program SoStar of the PSI2 project funded by the IDEX Paris-Saclay, ANR-11-IDEX-0003-02. The authors acknowledge Paris-Saclay University's Institut Pascal program "The Self-Organized Star Formation Process" and the Interstellar Institute for hosting discussions that nourished the development of the ideas behind this work. This work uses observations made with the NASA/ESA Hubble Space Telescope, obtained from the Data Archive at the Space Telescope Science Institute, which is operated by the Association of Universities for Research in Astronomy, Inc., under NASA contract NAS5-26555. These observations are associated with program 13448.

Facilities: WHAM, HST (COS)

Software: `astropy` (Robitaille et al. 2013), `matplotlib` (Hunter 2007), `seaborn` (Waskom et al. 2014), `whampy` (Krishnarao 2019), `lmfit` (Newville et al. 2019), `dustmaps` (Green 2018), `bettermoments` (Teague & Foreman-Mackey 2018), `emcee` (Foreman-Mackey et al. 2013).

REFERENCES

- Ackermann, M., Albert, A., Atwood, W. B., et al. 2014, ApJ, 793, 64, doi: [10.1088/0004-637X/793/1/64](https://doi.org/10.1088/0004-637X/793/1/64)
- Almy, R. C., McCammon, D., Digel, S. W., Bronfman, L., & May, J. 2000, ApJ, 545, 290, doi: [10.1086/317768](https://doi.org/10.1086/317768)
- Asplund, M., Grevesse, N., Sauval, A. J., & Scott, P. 2009, ARA&A, 47, 481, doi: [10.1146/annurev.astro.46.060407.145222](https://doi.org/10.1146/annurev.astro.46.060407.145222)
- Barger, K. A., Madsen, G. J., Fox, A. J., et al. 2017, ApJ, 851, 110, doi: [10.3847/1538-4357/aa992a](https://doi.org/10.3847/1538-4357/aa992a)
- Bland, J., & Tully, B. 1988, Nature, 334, 43, doi: [10.1038/334043a0](https://doi.org/10.1038/334043a0)
- Bland-Hawthorn, J., & Cohen, M. 2003, ApJ, 582, 246, doi: [10.1086/344573](https://doi.org/10.1086/344573)
- Bland-Hawthorn, J., & Gerhard, O. 2016, ARA&A, 54, 529, doi: [10.1146/annurev-astro-081915-023441](https://doi.org/10.1146/annurev-astro-081915-023441)
- Bland-Hawthorn, J., Maloney, P. R., Sutherland, R. S., & Madsen, G. J. 2013, ApJ, 778, 58, doi: [10.1088/0004-637X/778/1/58](https://doi.org/10.1088/0004-637X/778/1/58)
- Bland-Hawthorn, J., Maloney, P. R., Sutherland, R., et al. 2019, ApJ, 886, 45, doi: [10.3847/1538-4357/ab44c8](https://doi.org/10.3847/1538-4357/ab44c8)
- Bordoloi, R., Fox, A. J., Lockman, F. J., et al. 2017, ApJ, 834, 191, doi: [10.3847/1538-4357/834/2/191](https://doi.org/10.3847/1538-4357/834/2/191)
- Carretti, E., Crocker, R. M., Staveley-Smith, L., et al. 2013, Nature, 493, 66, doi: [10.1038/nature11734](https://doi.org/10.1038/nature11734)
- Cecil, G., Bland-Hawthorn, J., Veilleux, S., & Filippenko, A. V. 2001, ApJ, 555, 338, doi: [10.1086/321481](https://doi.org/10.1086/321481)
- Di Teodoro, E. M., McClure-Griffiths, N. M., Lockman, F. J., et al. 2018, ApJ, 855, 33, doi: [10.3847/1538-4357/aaad6a](https://doi.org/10.3847/1538-4357/aaad6a)

- Dobler, G., & Finkbeiner, D. P. 2008, *ApJ*, 680, 1222, doi: [10.1086/587862](https://doi.org/10.1086/587862)
- Dobler, G., Finkbeiner, D. P., Cholis, I., Slatyer, T., & Weiner, N. 2010, *ApJ*, 717, 825, doi: [10.1088/0004-637X/717/2/825](https://doi.org/10.1088/0004-637X/717/2/825)
- Draine, B. T. 2011, *Physics of the Interstellar and Intergalactic Medium*
- Finkbeiner, D. P. 2004, *ApJ*, 614, 186, doi: [10.1086/423482](https://doi.org/10.1086/423482)
- Fitzpatrick, E. L., & Massa, D. 2007, *ApJ*, 663, 320, doi: [10.1086/518158](https://doi.org/10.1086/518158)
- Foreman-Mackey, D., Hogg, D. W., Lang, D., & Goodman, J. 2013, *PASP*, 125, 306, doi: [10.1086/670067](https://doi.org/10.1086/670067)
- Fox, A. J., Wakker, B. P., Barger, K. A., et al. 2014, *ApJ*, 787, 147, doi: [10.1088/0004-637X/787/2/147](https://doi.org/10.1088/0004-637X/787/2/147)
- Fox, A. J., Bordoloi, R., Savage, B. D., et al. 2015, *ApJL*, 799, L7, doi: [10.1088/2041-8205/799/1/L7](https://doi.org/10.1088/2041-8205/799/1/L7)
- Green, G. M. 2018, *The Journal of Open Source Software*, 3, 695, doi: [10.21105/joss.00695](https://doi.org/10.21105/joss.00695)
- Green, G. M., Schlafly, E., Zucker, C., Speagle, J. S., & Finkbeiner, D. 2019, *ApJ*, 887, 93, doi: [10.3847/1538-4357/ab5362](https://doi.org/10.3847/1538-4357/ab5362)
- Green, J. C., Froning, C. S., Osterman, S., et al. 2012, *ApJ*, 744, 60, doi: [10.1088/0004-637X/744/1/60](https://doi.org/10.1088/0004-637X/744/1/60)
- Haffner, L. M., Reynolds, R. J., & Tufte, S. L. 1999, *ApJ*, 523, 223, doi: [10.1086/307734](https://doi.org/10.1086/307734)
- Haffner, L. M., Reynolds, R. J., Tufte, S. L., et al. 2003, *ApJS*, 149, 405, doi: [10.1086/378850](https://doi.org/10.1086/378850)
- Haffner, L. M., Reynolds, R. J., Madsen, G. J., et al. 2010, in *Astronomical Society of the Pacific Conference Series*, Vol. 438, *The Dynamic Interstellar Medium: A Celebration of the Canadian Galactic Plane Survey*, ed. R. Kothes, T. L. Landecker, & A. G. Willis, 388. <https://arxiv.org/abs/1008.0612>
- Heckman, T. M. 2002, *Astronomical Society of the Pacific Conference Series*, Vol. 254, *Galactic Superwinds Circa 2001*, ed. J. S. Mulchaey & J. T. Stocke, 292
- Hunter, J. D. 2007, *Computing in Science & Engineering*, 9, 90, doi: [10.1109/MCSE.2007.55](https://doi.org/10.1109/MCSE.2007.55)
- Karim, M. T., Fox, A. J., Jenkins, E. B., et al. 2018, *ApJ*, 860, 98, doi: [10.3847/1538-4357/aac167](https://doi.org/10.3847/1538-4357/aac167)
- Keeney, B. A., Danforth, C. W., Stocke, J. T., et al. 2006, *ApJ*, 646, 951, doi: [10.1086/505128](https://doi.org/10.1086/505128)
- Krishnarao, D. 2019, *The Journal of Open Source Software*, 4, 1940, doi: [10.21105/joss.01940](https://doi.org/10.21105/joss.01940)
- Liszt, H. S., & Burton, W. B. 1980, *ApJ*, 236, 779, doi: [10.1086/157803](https://doi.org/10.1086/157803)
- Lockman, F. J., Di Teodoro, E. M., & McClure-Griffiths, N. M. 2020, *ApJ*, 888, 51, doi: [10.3847/1538-4357/ab55d8](https://doi.org/10.3847/1538-4357/ab55d8)
- McClure-Griffiths, N. M., Green, J. A., Hill, A. S., et al. 2013, *ApJL*, 770, L4, doi: [10.1088/2041-8205/770/1/L4](https://doi.org/10.1088/2041-8205/770/1/L4)
- Miller, M. J., & Bregman, J. N. 2015, *ApJ*, 800, 14, doi: [10.1088/0004-637X/800/1/14](https://doi.org/10.1088/0004-637X/800/1/14)
- . 2016, *ApJ*, 829, 9, doi: [10.3847/0004-637X/829/1/9](https://doi.org/10.3847/0004-637X/829/1/9)
- Newville, M., Otten, R., Nelson, A., et al. 2019, *lmfit/lmfit-py* 1.0.0, 1.0.0, Zenodo, doi: [10.5281/zenodo.3588521](https://doi.org/10.5281/zenodo.3588521)
- Oort, J. H. 1977, *ARA&A*, 15, 295, doi: [10.1146/annurev.aa.15.090177.001455](https://doi.org/10.1146/annurev.aa.15.090177.001455)
- Robitaille, T. P., Tollerud, E. J., Greenfield, P., et al. 2013, *Astronomy & Astrophysics*, 558, A33, doi: [10.1051/0004-6361/201322068](https://doi.org/10.1051/0004-6361/201322068)
- Sahan, M., & Haffner, L. M. 2016, *AJ*, 151, 147, doi: [10.3847/0004-6256/151/6/147](https://doi.org/10.3847/0004-6256/151/6/147)
- Savage, B. D., Kim, T.-S., Fox, A. J., et al. 2017, *ApJS*, 232, 25, doi: [10.3847/1538-4365/aa8f4c](https://doi.org/10.3847/1538-4365/aa8f4c)
- Savitzky, A., & Golay, M. J. E. 1964, *Analytical Chemistry*, 36, 1627
- Sembach, K. R., Howk, J. C., Ryans, R. S. I., & Keenan, F. P. 2000, *ApJ*, 528, 310, doi: [10.1086/308173](https://doi.org/10.1086/308173)
- Snowden, S. L., Egger, R., Freyberg, M. J., et al. 1997, *ApJ*, 485, 125, doi: [10.1086/304399](https://doi.org/10.1086/304399)
- Sofue, Y. 2000, *ApJ*, 540, 224, doi: [10.1086/309297](https://doi.org/10.1086/309297)
- Sormani, M. C., Treß, R. G., Ridley, M., et al. 2018, *MNRAS*, 475, 2383, doi: [10.1093/mnras/stx3258](https://doi.org/10.1093/mnras/stx3258)
- Su, M., Slatyer, T. R., & Finkbeiner, D. P. 2010, *ApJ*, 724, 1044, doi: [10.1088/0004-637X/724/2/1044](https://doi.org/10.1088/0004-637X/724/2/1044)
- Teague, R., & Foreman-Mackey, D. 2018, *Research Notes of the American Astronomical Society*, 2, 173, doi: [10.3847/2515-5172/aae265](https://doi.org/10.3847/2515-5172/aae265)
- Veilleux, S., & Rupke, D. S. 2002, *ApJL*, 565, L63, doi: [10.1086/339226](https://doi.org/10.1086/339226)
- Waskom, M., Botvinnik, O., Hobson, P., et al. 2014, doi: [10.5281/ZENODO.12710](https://doi.org/10.5281/ZENODO.12710)